Research Square

Preprints are preliminary reports that have not undergone peer review.
They should not be considered conclusive, used to inform clinical practice,
or referenced by the media as validated information.

PAPR Control in Digital Predistortion Systems Using PC-CFR and RLS Forgetting Factor Adjustment

Xin Wan
Communication University of China
Ruiyang Liu
Communication University of China
Fei Yang
yangsher@cuc.edu.cn
Communication University of China
Yanan Luo
Communication University of China
Yu Ye
Communication University of China

Research Article

Keywords: digital predistortion, peak-cancellation CFR, recursive least squares, power amplifier linearization, PAPR control

Posted Date: November 2nd, 2026

DOI: https://doi.org/10.21203/rs.3.rs-11090468/v1

License: This work is licensed under a Creative Commons Attribution 4.0 International License.
Read Full License

Additional Declarations: No competing interests reported.

PAPR Control in Digital Predistortion Systems Using PC-CFR and RLS Forgetting Factor Adjustment

Xin Wan[1], Ruiyang Liu[1], Fei Yang[1*], Yanan Luo[1], Yu Ye[1]

[1]Communication University of China, No. 1 Dingfuzhuang East Street, Chaoyang District, Beijing, 100024, China.

*Corresponding author(s). E-mail(s): yangsher@cuc.edu.cn;
Contributing authors: wallin82@cuc.edu.cn; liury2003@outlook.com; luoya@cuc.edu.cn; yeyurain2020@163.com;

Abstract

The high peak-to-average power ratio (PAPR) of orthogonal frequency-division multiplexing (OFDM) signals presents a challenge for power amplifier (PA) linearization. Cascaded crest factor reduction (CFR) and digital predistortion (DPD) suppress signal peaks and compensate for PA nonlinearity, but unsuitable parameter settings can cause excessive waveform distortion or peak regrowth after predistortion. This paper investigates the joint adjustment of peak-cancellation CFR (PC-CFR) and recursive least-squares (RLS) identification to control DPD-output PAPR while preserving linearization performance. The PC-CFR threshold determines the distortion introduced before predistortion, whereas the RLS forgetting factor influences coefficient adaptation and subsequent peak regrowth. A sequential procedure first determines the target PAPR immediately before normalized mean-square error (NMSE) first worsens and then selects the lowest-NMSE forgetting factor satisfying the PAPR constraint. Experimental results show that joint adjustment reduces DPD-output PAPR from 12.985 to 11.593 dB and improves PA feedback NMSE from -34.877 to -38.537 dB. The adjacent-channel power ratio (ACPR) in the upper and lower channels improves from -49.370/-50.332 to -51.923/-52.747 dBc. These results demonstrate coordinated peak suppression and improved linearization for the measured operating condition.

Keywords: digital predistortion, peak-cancellation CFR, recursive least squares, power amplifier linearization, PAPR control

1 Introduction

Orthogonal frequency-division multiplexing (OFDM) signals are widely used in modern wireless transmitters, but they have a high peak-to-average power ratio (PAPR) because of constructive interference among subcarriers [1–3]. High PAPR increases the likelihood that the power amplifier (PA) will operate in a nonlinear region unless sufficient input back-off is applied, which reduces power efficiency and complicates transmitter design [4–6]. In practice, excessive peaks are also associated with in-band distortion and spectral regrowth, and they can trigger hardware limitations such as digital-front-end clipping or deep PA saturation, thereby degrading error metrics and adjacent-channel emission [7–11].

To address PA linearization under strict peak constraints, cascading crest factor reduction (CFR) with digital predistortion (DPD) is a practical solution [4–6, 12, 13]. CFR suppresses instantaneous peaks in the baseband signal to provide margin for the later predistortion stage, whereas DPD compensates PA nonlinearity by applying an inverse behavioral response to the input signal [8, 12, 14–16]. Among CFR approaches, peak-cancellation CFR (PC-CFR) is particularly attractive because it uses band-limited cancellation pulses and can effectively suppress peaks with low implementation cost and limited spectral regrowth [1, 7, 17–19].

In a transmitter using CFR and DPD, the resulting PA input PAPR is affected by the parameter settings of both stages. If the parameters in either the CFR stage or the DPD identification process are not chosen properly, the predistorted signal may exhibit large peak regrowth after DPD. On the CFR side, parameter selection determines the trade-off between peak-reduction capability and the distortion introduced into the

signal, and thus directly affects the resulting PAPR [5, 6, 13–15, 20]. On the DPD side, the identification settings also influence the envelope of the predistorted signal. In recursive least-squares (RLS)-based identification, for example, the forgetting factor controls the weighting of past observations [21, 22]. An inappropriate forgetting factor can lead to stronger coefficient fluctuations during adaptation and therefore increase instantaneous peaks in the predistorted signal [23–25].

This paper investigates DPD-output PAPR control by coordinating the PC-CFR threshold and RLS forgetting factor. Here, DPD-output PAPR means the PAPR of the digital signal sent to the radio-frequency (RF) chain after DPD. The digital studies characterize the waveform distortion of stronger cancellation and the configuration-dependent effect of the forgetting factor on peak regrowth. When the default trigger is exceeded, the proposed procedure selects the target PAPR immediately before normalized mean-square error (NMSE) first worsens, then selects the forgetting factor with the lowest NMSE under the PAPR constraint. The adjacent-channel power ratio (ACPR) is evaluated separately in the upper and lower channels alongside NMSE to identify the cost of stronger cancellation. The field-programmable gate array (FPGA) implements CFR and DPD, while the personal computer (PC) controls the threshold and identifies the coefficients. In the hardware experiment, the method reduces DPD-output PAPR from 12.985 to 11.593 dB, improves PA feedback NMSE by 3.660 dB, and improves upper and lower ACPR by 2.554/2.416 dB. The default trigger is 12.5 dB and is updated to 12.593 dB after adjustment. These measurements illustrate the procedure under fixed PA input-power and gain settings.

2 Methods: Peak-Cancellation CFR

Among the CFR methods used in transmitter chains, PC-CFR provides a practical balance between peak suppression, adjacent-channel leakage suppression, and implementation complexity. Unlike direct clipping followed by filtering, PC-CFR reduces

selected peaks by subtracting spectrally shaped cancellation pulses. The pulse coefficients can be prepared in advance, and the online processing is dominated by peak detection, scaling, alignment, and subtraction, which makes the method suitable for real-time implementation in an FPGA.

2.1 Principle and Architecture

The PC-CFR operation consists of three coordinated stages. First, the magnitude of the complex baseband signal is compared with a predefined threshold. Samples above the threshold are treated as peak candidates, and a sliding search window retains the local maximum in each peak region. This local-maximum selection avoids adding several cancellation pulses into adjacent samples that belong to the same physical peak.

Second, a cancellation pulse is generated for every detected peak. Its amplitude is proportional to the excess magnitude above the threshold, while its phase is aligned with the instantaneous phase of the selected sample so that the pulse is subtracted coherently. The pulse waveform is implemented as a finite impulse response (FIR) sequence derived from a band-limited filter design. Because the coefficients are calculated in advance and stored in the hardware, the added cancellation energy can be confined mainly to the occupied signal band without an online filter-design step.

Third, the scaled and phase-aligned pulse is subtracted from a delayed copy of the main signal at the corresponding sample position. The delay compensates for the latency of magnitude extraction, peak selection, and pulse generation. The operation is localized around the detected peaks, so samples outside those regions remain largely unchanged. The combination of time localization and spectral shaping suppresses instantaneous peaks while limiting the in-band and out-of-band disturbance introduced by the cancellation process.

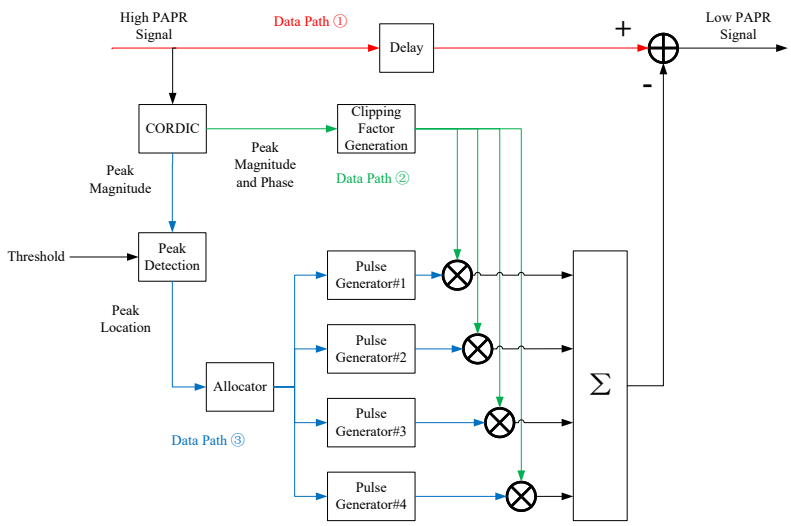


Fig. 1 PC-CFR hardware architecture. Schematic diagram of a typical PC-CFR hardware architecture, including the main delay path, peak detection and scaling path, and pulse generation path.

Figure 1 shows the corresponding hardware structure. The main path buffers the input samples to match the processing latency. In parallel, the detection and scaling path extracts magnitude and phase, compares the magnitude with the threshold, and calculates the required cancellation amplitude. A coordinate rotation digital computer (CORDIC) unit can be used for real-time magnitude and phase extraction. The pulse-generation path then produces the stored FIR sequence and applies the calculated complex scale. The delayed main signal and the cancellation path must be aligned before subtraction; otherwise, the pulse may fail to suppress the intended peak or may create a new local maximum.

Figure 2(a) compares the input and output envelopes. Only the regions surrounding detected peaks are modified, and their magnitudes are reduced toward the configured threshold. Figure 2(b) shows the cancellation pulses aligned with the detected peak positions. Accurate time and phase alignment enables coherent subtraction and prevents unnecessary disturbance of neighboring samples. This localized, band-limited operation distinguishes PC-CFR from direct amplitude clipping.

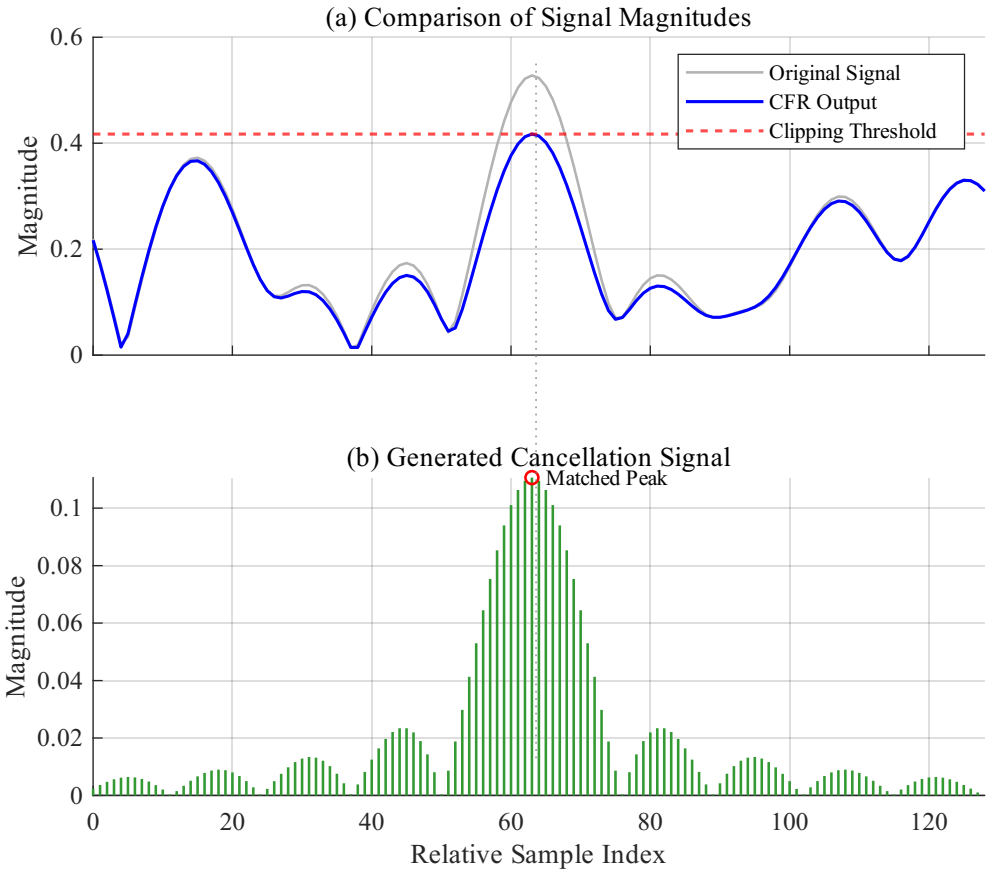


Fig. 2 Time-domain behavior of PC-CFR. Time-domain behavior of the PC-CFR scheme. (a) Envelope comparison between input and output signals, showing peak suppression near the threshold. (b) Cancellation pulses aligned with detected peak locations.

The cancellation pulse is obtained from a symmetric low-pass FIR design. The positive-frequency passband and stopband edges are denoted by f_{p} and f_{s}, respectively; the negative-frequency response is symmetric. For the pulse used in the digital study below, $f_{\mathrm{p}} = 4.5$ MHz and $f_{\mathrm{s}} = 4.75$ MHz at a sampling rate of 122.88 MHz. The stopband edge matches the lower edge of the adjacent-channel integration band. Figure 3 shows how increasing the FIR order sharpens this transition. The implemented order is $L = 1024$, corresponding to 1025 taps.

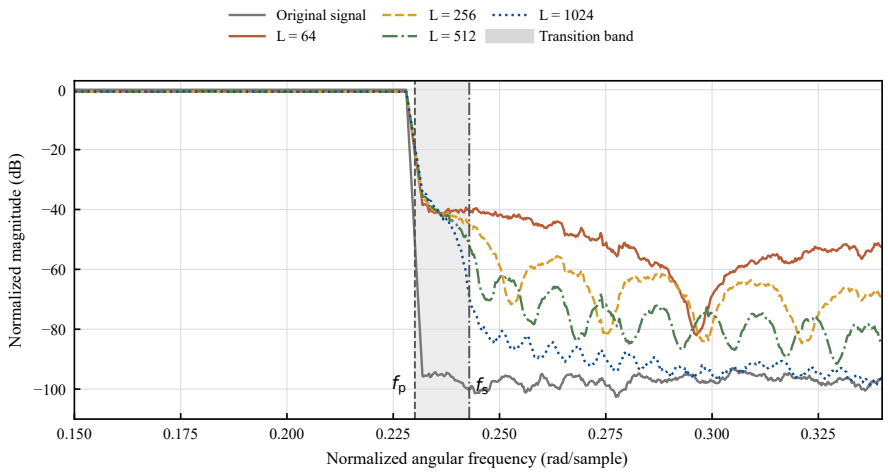


Fig. 3 Cancellation-pulse filter order and output spectra. Normalized spectra of the original signal and PC-CFR output signals for different cancellation-pulse filter orders. L denotes the FIR order; f_p and f_s mark the 4.5 MHz passband edge and the 4.75 MHz stopband edge, respectively, on the normalized angular-frequency axis. The stopband edge coincides with the start of adjacent-channel integration.

2.2 Waveform-Relative PC-CFR Threshold and the NMSE–ACPR Trade-Off

Let $P_{\mathrm{in},i}$ denote the measured PAPR of waveform i, and let ΔP denote the requested PAPR reduction. Here, target PAPR refers to the PAPR requested for the CFR output, in decibels, not the amplitude threshold used by the peak detector. The target PAPR for that waveform is set to $\tau_i = P_{\mathrm{in},i} - \Delta P$. Each target PAPR is set below the corresponding input PAPR to evaluate the effect of increasing peak reduction. Increasing ΔP lowers the cancellation threshold and therefore increases the number and magnitude of cancellation pulses. This section quantifies the resulting changes in CFR waveform NMSE and ACPR.

The relation was quantified with 300 independently generated quadrature phase-shift keying (QPSK) OFDM waveforms. Each waveform contained 24576 complex samples at 122.88 MHz. The requested reductions were $\Delta P \in \{0.5, 1, 1.5, 2, 2.5, 3\}$ dB. The 1025-tap least-squares pulse, 20-sample peak-detection window, one cancellation

iteration, and 16 pulse generators were fixed. To preserve complete cancellation pulses at the packet boundaries, three identical copies of each waveform were processed jointly and all metrics were evaluated only on the middle copy. The same waveform set was used at every reduction level, so comparisons were paired by waveform.

The measured CFR-output PAPR is calculated from the maximum instantaneous power and the mean power of the processed waveform. CFR waveform NMSE is the error-energy ratio relative to the unmodified OFDM waveform without complex-gain fitting. The 10th and 90th percentiles are denoted by Q10 and Q90. Waveform percentiles are calculated in the linear power-ratio domain before conversion to decibels.

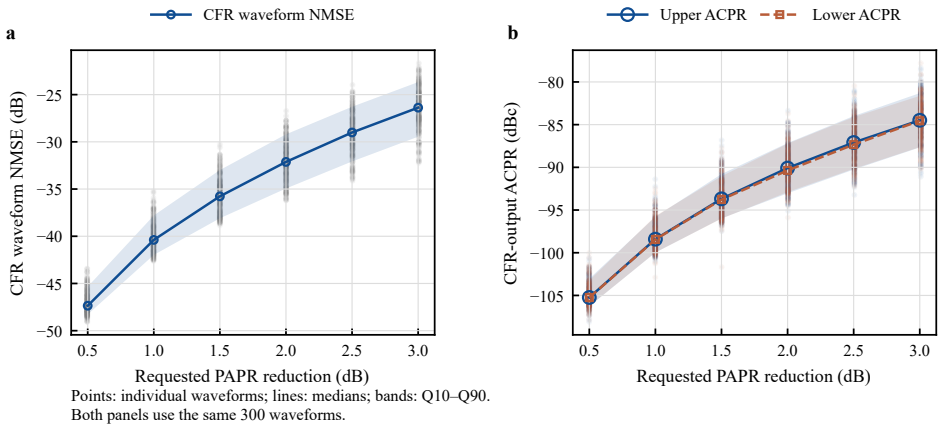


Fig. 4 CFR distortion and adjacent-channel leakage. CFR waveform NMSE and ACPR for waveform-relative target PAPR levels. (a) CFR waveform NMSE without gain fitting. (b) Upper and lower CFR-output ACPR. The target for each waveform is its measured input PAPR minus the requested reduction. Points show all 300 paired waveforms at each setting; lines and bands show the median and Q10–Q90 waveform range, respectively.

The waveform distortion increases with the requested reduction (Figure 4). The median achieved reduction increased from 0.497 to 2.835 dB across the six settings, while the CFR waveform NMSE Q90 deteriorated from −45.341 to −23.671 dB. The two ACPR sides also became less negative because stronger cancellation increases

the total cancellation-error power. However, the pulse itself provides an integrated adjacent-channel suppression of 57.786 dB under the same measurement bands, so the CFR-output ACPR remains approximately 58 dB below the CFR waveform NMSE. As a result, both ACPR Q90 values remained below −81.3 dBc even at the strongest setting. These results show that CFR waveform NMSE is the immediate limitation of stronger peak reduction, whereas adjacent-channel leakage remains largely suppressed by the band-aligned cancellation pulse. Table 1 summarizes all six relative-reduction settings.

Table 1 Digital PC-CFR results at six waveform-relative PAPR-reduction levels.

Requested reduction (dB)	Achieved reduction median [Q10, Q90] (dB)	NMSE Q90 (dB)	Lower ACPR Q90 (dBc)	Upper ACPR Q90 (dBc)
0.5	0.497 [0.492, 0.498]	−45.341	−103.237	−103.036
1.0	0.988 [0.971, 0.995]	−37.797	−95.695	−95.791
1.5	1.473 [1.438, 1.490]	−32.988	−91.040	−90.789
2.0	1.949 [1.889, 1.978]	−29.205	−87.230	−87.158
2.5	2.405 [2.279, 2.457]	−26.284	−84.114	−83.991
3.0	2.835 [2.581, 2.926]	−23.671	−81.637	−81.310

3 Methods: DPD Algorithm Design

DPD compensates for PA nonlinearity by shaping the signal before amplification. This operation can also increase the signal peaks. The amount of peak regrowth depends in part on the coefficient identification process. This section describes the RLS-based DPD algorithm and then quantifies the relation between its constant forgetting factor and the PAPR of the DPD output signal.

3.1 RLS Algorithm Principle

The DPD uses an indirect learning architecture. A postdistorter, which estimates the PA input from the PA output, is first fitted to the measured signal pair. Its coefficients are then copied to the predistorter. A memory polynomial model is used because it can represent both nonlinear and memory effects with moderate complexity. The estimated PA input is

$$\hat{z}[n] = \sum_{k=1}^{K} \sum_{q=0}^{Q} a_{kq} \cdot |y[n-q]|^{k-1} \cdot y[n-q], \tag{1}$$

where $y[n]$ is the PA output, K is the nonlinear order, Q is the memory depth, and a_{kq} is a model coefficient. With the coefficient vector $\mathbf{a}$ and basis-function vector $\boldsymbol{\phi}[n]$, the model can be written as $\hat{z}[n] = \boldsymbol{\phi}^T[n]\mathbf{a}$.

Batch least squares estimates the coefficients from a fixed data block. RLS instead updates the estimate as each sample is processed. It minimizes the exponentially weighted error

$$J[n] = \sum_{i=1}^{n} \lambda^{n-i} |e[i]|^2, \tag{2}$$

where $e[i] = z[i] - \hat{z}[i]$ is the estimation error. The forgetting factor λ satisfies $0 < \lambda \leq 1$. It controls how quickly the weight assigned to older samples decreases.

The matrix inversion lemma gives the following recursive updates:

$$\begin{aligned} \mathbf{k}[n] &= \frac{\mathbf{R}^{-1}[n-1]\boldsymbol{\phi}[n]}{\lambda + \boldsymbol{\phi}^H[n]\mathbf{R}^{-1}[n-1]\boldsymbol{\phi}[n]}, \\ e[n] &= z[n] - \boldsymbol{\phi}^T[n]\mathbf{a}[n-1], \\ \mathbf{a}[n] &= \mathbf{a}[n-1] + \mathbf{k}[n]e^*[n], \\ \mathbf{R}^{-1}[n] &= \frac{1}{\lambda}\Big(\mathbf{R}^{-1}[n-1] - \mathbf{k}[n]\boldsymbol{\phi}^H[n]\mathbf{R}^{-1}[n-1]\Big). \end{aligned} \tag{3}$$

where $\mathbf{k}[n]$ is the gain vector and $e[n]$ is the a priori prediction error, evaluated using the coefficients before the current update. The inverse correlation matrix is initialized as $\mathbf{R}^{-1}[0] = \delta^{-1}\mathbf{I}$. The coefficient vector is initialized as $\mathbf{a}[0] = [1, 0, \ldots, 0]^T$.

3.2 RLS Forgetting Factor and DPD-Output PAPR

The forgetting factor determines the weighting of past observations, with an approximate effective memory length of $1/(1-\lambda)$ samples. Its selection changes the identified inverse response and therefore the peaks generated by DPD. This section examines the reduction in peak regrowth as the forgetting factor increases over the evaluated range.

An offline study used an aligned input and PA feedback signal pair acquired with a fixed 7 dB target PAPR. The input contains 24576 samples, and the model is a fifth-order memory polynomial with five memory taps. The waveform, model, initial coefficients, and identification interval were held fixed. The factors span 0.9–0.9999, sampled on $u = -\log_{10}(1-\lambda)$, with the three practical levels explicitly included. To evaluate the broad range without covariance-update numerical breakdown, the exponentially weighted least-squares objective was implemented using square-root QR updates.

Figure 5 shows that DPD-output PAPR decreases monotonically as the forgetting factor increases. PAPR falls from 12.391 dB at $\lambda = 0.9$ to 7.808 dB at $\lambda = 0.9999$, a reduction of 4.583 dB. A small forgetting factor therefore produces large peak regrowth in this experiment. The three factors 0.999, 0.9995, and 0.9999 yield 7.8248, 7.8193, and 7.8076 dB, respectively. Their total variation is only 0.0172 dB, indicating a much flatter response in this region. The inset resolves these small differences.

The three practical levels cover effective memory lengths of approximately 1000, 2000, and 10000 samples. Their small PAPR variation motivates using these three levels for finer adjustment after the strong peak regrowth associated with small forgetting factors has been suppressed. A larger factor retains more historical information and

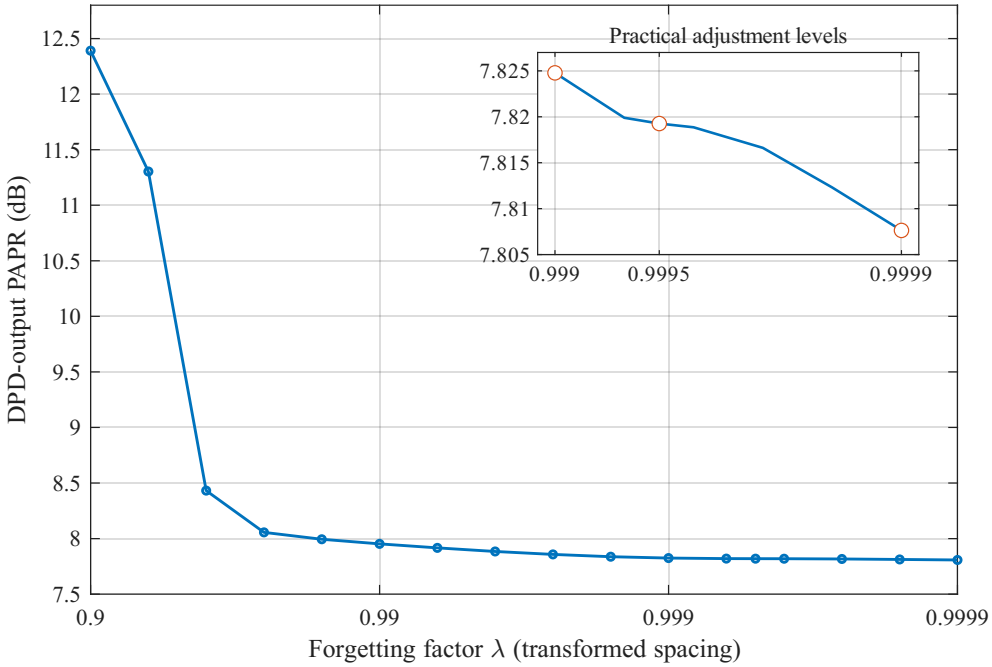


Fig. 5 Forgetting factor and DPD-output PAPR. DPD-output PAPR versus the RLS forgetting factor, with a magnified view of the three practical adjustment levels. The horizontal axes use the transformed coordinate $u = -\log_{10}(1-\lambda)$ and display the corresponding forgetting factors.

may respond more slowly to changing conditions. The PAPR response depends on the PA operating condition and input waveform. The observed decreasing trend guides forgetting-factor adjustment, with the final factor selected from measured PAPR and NMSE.

4 Methods: Joint PC-CFR and RLS Parameter Adjustment

Sections 2.2 and 3.2 identify two distinct mechanisms for controlling peak regrowth. PC-CFR directly modifies the waveform; stronger cancellation can impose a large increase in CFR waveform NMSE even when its adjacent-channel leakage remains small. The RLS forgetting factor changes the identified predistorter and its peak regrowth, with a response that depends on the input and PA operating condition.

A longer effective memory length need not worsen steady-state NMSE, although it reduces responsiveness to changes. The two parameters are therefore selected using measured PAPR, NMSE, and ACPR.

The method uses a trigger threshold P_{trig} that also constrains the final DPD-output PAPR. The trigger threshold is set for the operating condition. Exceeding this threshold initiates adjustment; merely crossing below it does not terminate the search. The following three steps separate target PAPR selection from forgetting-factor adjustment.

1. **Configure the levels and activate adjustment.** Use the digital studies to bound the target PAPR levels and forgetting factors. Arrange target PAPR levels in descending order with uniform spacing and distribute the forgetting factors over the effective memory-length range, using logarithmic spacing as a design guide. Measure the current DPD-output PAPR. Retain the current configuration when the trigger is inactive. Otherwise, set the forgetting factor to the lowest available level and begin CFR evaluation. Skip any target PAPR that is not below the original input PAPR, since that level does not request actual peak suppression.
2. **Locate the onset of NMSE degradation.** At the lowest forgetting factor, progressively lower the target PAPR, identify the DPD coefficients, and measure DPD-output PAPR and PA feedback NMSE and upper and lower ACPR at each level. Continue while NMSE improves. At the first deterioration relative to the preceding level, retain the preceding target PAPR. Crossing the PAPR threshold alone does not stop this stage: stronger cancellation may improve adjacent-channel leakage suppression while degrading reconstruction of the original waveform. This stopping rule limits that additional waveform distortion.
3. **Adjust the forgetting factor and update the trigger.** Fix the retained target PAPR and evaluate the available forgetting factors. Check the expected decreasing trend of DPD-output PAPR as the forgetting factor increases; a violation requires

re-evaluation before the result is accepted. Among the factors whose measured PAPR is below P_{trig}, retain the one with the lowest PA feedback NMSE. Evaluate upper and lower ACPR alongside NMSE when comparing the settings. If no factor meets the PAPR constraint, no final setting is accepted. After a final setting is accepted, update the trigger to its measured DPD-output PAPR plus a positive trigger margin ΔP_{trig} for subsequent operation.

The updated threshold is used for subsequent parameter adjustment. Hardware measurements in Section 5 illustrate the procedure using an explicitly stated operating threshold and report the measured benefit relative to the same initial DPD configuration.

5 Experimental Results

5.1 Experimental Setup

The PC–MATLAB block generates the complex OFDM waveform and performs parameter adjustment. Both sample-by-sample CFR and DPD processing are implemented in the FPGA. MATLAB computes the CFR amplitude threshold from the requested target and the reference mean power, and transfers the threshold and cancellation-pulse coefficients to the FPGA. It also aligns the captured signals, performs RLS-based DPD coefficient identification, converts the coefficients into lookup table (LUT) contents, and loads the FPGA DPD tables through the control interface. Thus, the FPGA implements the transmit datapath, while CFR threshold control and RLS coefficient calculation reside on the PC. Figure 6 shows the experimental DPD platform.

The FPGA output enters the transceiver (ADRV9009), whose transmit (Tx) path drives the preamplifier (AH202) followed by the 50 W PA device under test (DUT). The PA feedback path passes through the 11 dB attenuator to the transceiver receive

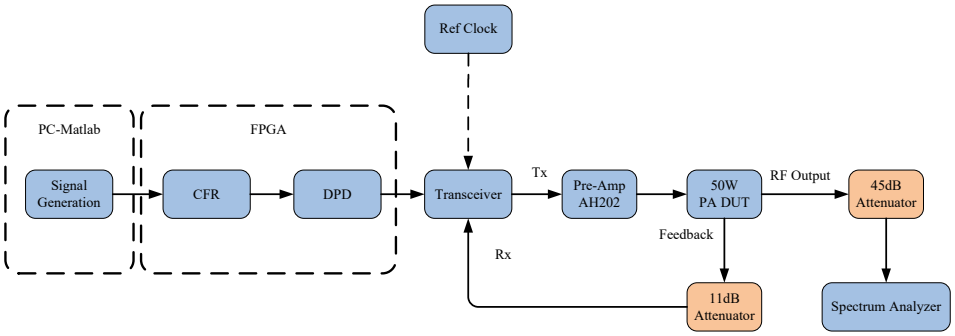


Fig. 6 Experimental platform signal flow. Signal flow of the experimental DPD platform. CFR and DPD operate in the FPGA; threshold control and RLS identification operate in PC–MATLAB.

(Rx) input. A separate RF output path passes through the 45 dB attenuator to the spectrum analyzer. The Ref Clock supplies the transceiver reference. Figure 7 identifies these components together with the PC, FPGA, Power Supply I, and Power Supply II. The PA input-power and gain settings are held fixed throughout the measurements; the digital mean-power reference is unchanged while CFR and DPD reshape the signal peaks.

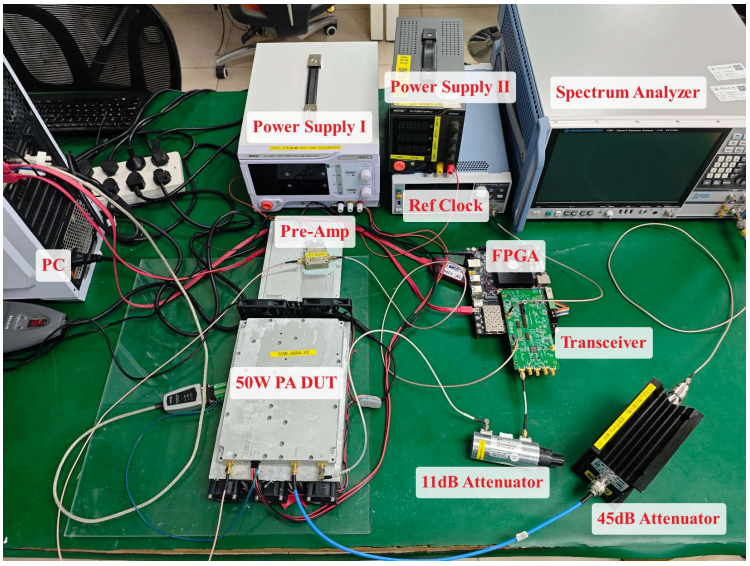


Fig. 7 PA measurement hardware. Hardware used for the PA measurements. Component names correspond to the signal-flow diagram.

Each hardware transmission uses a QPSK OFDM waveform containing 24576 complex samples at 122.88 MS/s. A fixed mean-power reference is used throughout parameter adjustment. The unmodified waveform is scaled to this reference before CFR, and the same reference waveform is retained for end-to-end NMSE evaluation.

The hardware CFR uses a peak-normalized, symmetric, least-squares FIR cancellation pulse with 1025 taps. Its passband edge is 4.5 MHz and its stopband starts at 4.75 MHz, matching the lower edge of adjacent-channel integration. Only the cancellation threshold changes during adjustment; the pulse remains fixed. The DPD uses the configured sparse envelope/signal-delay LUT basis with 190 complex coefficients. The selected basis spans delays from zero to seven samples and envelope powers from zero to nine. LUT generation uses 512 entries per branch, with 16-bit real and imaginary components and 11 fractional bits. Table 2 summarizes the fixed waveform, hardware, and signal-processing settings used throughout the measurements.

Table 2 Fixed Experimental Settings

Parameter	Value
Waveform	QPSK OFDM
Transmit and acquisition sample rate	122.88 MS/s
Samples per hardware transmission	24576
Oversampling factor	12
PA input-power and gain settings	Fixed
RLS identification length	10000 samples
DPD basis	190 complex coefficients
DPD LUT depth	512 entries per branch
LUT component representation	16 bits, including 11 fractional bits
CFR pulse	Least-squares FIR, 1025 taps
CFR passband / stopband edge	4.5 / 4.75 MHz
Main-channel integration bandwidth	9.3 MHz

At each CFR setting, the DPD is first bypassed to acquire the CFR output and corresponding PA feedback for coefficient identification. The captured pair is aligned in delay, gain, and phase, and RLS processes 10000 samples. After loading the resulting

DPD LUTs, the corrected waveform is transmitted and the system waits 5 s before acquisition. The captured PA feedback after DPD correction is aligned against the DPD output signal, since these signals define the input and output of the RF chain. The final NMSE is then evaluated against the original, unmodified reference waveform.

In this section, PAPR denotes DPD-output PAPR unless another signal is specified. NMSE and ACPR describe the PA feedback signal, with the correction state stated for each comparison. ACPR is the integrated adjacent-channel power divided by the main-channel power, with upper and lower sides evaluated separately. More negative NMSE and ACPR indicate better performance. The spectrum analyzer monitors the RF output; the numerical ACPR values reported here are calculated from the captured complex feedback samples.

5.2 Joint Adjustment and Measured Results

The CFR waveform distortion measured in Section 2.2 motivates progressively testing mild cancellation before accepting stronger waveform distortion. The target PAPR levels used in the hardware experiment are 10, 9, 8, and 7 dB, providing 1 dB steps. The comparatively moderate PAPR variation in the high-forgetting-factor region of Section 3.2 motivates evaluating the levels 0.999, 0.9995, and 0.9999. Their effective memory lengths are approximately 1000, 2000, and 10000 samples.

The experiment uses an original input PAPR of 10.240 dB. Before DPD correction, PA feedback NMSE is -27.115 dB and upper and lower ACPR are $-34.586/-37.570$ dBc. The default adjustment trigger is 12.5 dB. It defines both the activation condition and the final PAPR constraint for this experiment. The subsequent trigger margin is 1 dB. Each parameter configuration was measured once. Table 3 reports the complete parameter response for this input.

With CFR bypassed and $\lambda = 0.999$, DPD increases PAPR to 12.985 dB, exceeding the 12.5 dB trigger and activating adjustment. At the same forgetting factor, the

Table 3 Measured parameter response in the joint-adjustment experiment.

Target PAPR (dB)	λ	CFR-output PAPR	DPD-output PAPR	PA feedback NMSE	Upper ACPR	Lower ACPR
Bypass	0.999	10.240	12.985	-34.877	-49.370	-50.332
Bypass	0.9995	10.240	12.248	-37.084	-50.795	-52.005
Bypass	0.9999	10.240	11.999	-38.097	-51.299	-52.073
10	0.999	10.002	12.498	-35.791	-49.786	-51.049
10	0.9995	10.002	11.842	-37.563	-51.424	-52.789
10	**0.9999**	**10.002**	**11.593**	**-38.537**	**-51.923**	**-52.747**
9	0.999	9.015	10.443	-35.576	-53.751	-55.035
9	0.9995	9.015	10.333	-35.614	-54.276	-55.006
9	0.9999	9.015	10.109	-35.071	-52.032	-52.648
8	0.999	8.035	9.238	-31.027	-56.128	-56.702
8	0.9995	8.035	9.134	-31.155	-57.534	-58.375
8	0.9999	8.035	8.952	-30.964	-57.069	-57.255
7	0.999	7.097	7.937	-26.962	-58.299	-59.042
7	0.9995	7.097	7.844	-26.934	-57.980	-59.124
7	0.9999	7.097	7.739	-26.836	-58.051	-58.025

PAPR and NMSE are in dB; ACPR is in dBc. The final setting is emphasized in bold.

10 dB target PAPR reduces PAPR to 12.498 dB, improves NMSE by 0.915 dB, and improves upper and lower ACPR by 0.416/0.717 dB. The method then evaluates the next CFR level to locate the onset of NMSE degradation. At the next target, 9 dB, NMSE deteriorates from -35.791 to -35.576 dB, although ACPR becomes more negative. The method therefore returns to the 10 dB target and proceeds to forgetting-factor adjustment. The 8 and 7 dB responses further illustrate the cost of excessive cancellation: low adjacent-channel power coexists with large error relative to the original waveform.

At the retained 10 dB target, increasing λ from 0.999 through 0.9995 to 0.9999 reduces DPD-output PAPR monotonically from 12.498 through 11.842 to 11.593 dB. All three settings satisfy the 12.5 dB PAPR constraint in the recorded measurements, and their NMSE values are -35.791, -37.563, and -38.537 dB. The final factor is therefore 0.9999. The lower-side ACPR changes slightly from -52.789 to

−52.747 dBc in the last step. Both final sides nevertheless improve relative to the initial configuration.

Relative to bypassed CFR at $\lambda = 0.999$, the final setting reduces PAPR by 1.392 dB and improves NMSE by 3.660 dB. Upper and lower ACPR improve by 2.554 and 2.416 dB, respectively. Relative to the original uncorrected PA response, the final NMSE improvement is 11.422 dB. The updated trigger is 12.593 dB, obtained by adding the 1 dB trigger margin to the final PAPR of 11.593 dB. This update applies to subsequent operation; the accepted result already satisfies the 12.5 dB threshold used for the present adjustment.

Reducing PAPR below the selected value requires balancing waveform reconstruction against adjacent-channel suppression. At $\lambda = 0.9999$, changing the target PAPR from 10 to 9 dB reduces PAPR by another 1.484 dB, but worsens NMSE by 3.466 dB; upper ACPR improves by only 0.109 dB and lower ACPR worsens by 0.100 dB. At a 7 dB target, much lower PAPR and adjacent-channel power coexist with NMSE of −26.836 dB. Thus, neither minimum PAPR nor minimum ACPR alone identifies the operating point. The adopted rule retains the lowest NMSE that meets the PAPR constraint at the retained target PAPR and reports upper and lower ACPR.

Figure 8(a) compares the digital signals entering the RF chain before correction, with DPD before adjustment, and after joint adjustment. Each curve is the complementary cumulative distribution function (CCDF) of sample power normalized to that signal's own mean power. The largest observed ratios are 10.240, 12.985, and 11.593 dB, respectively. Joint adjustment suppresses the DPD-generated tail.

Figure 8(b) compares the corresponding PA feedback spectra. The spectra are normalized to their peak levels. Both DPD states suppress the strong spectral regrowth of the uncorrected PA response, and joint adjustment further improves both adjacent-channel ratios relative to the initial DPD state. The displayed smoothed,

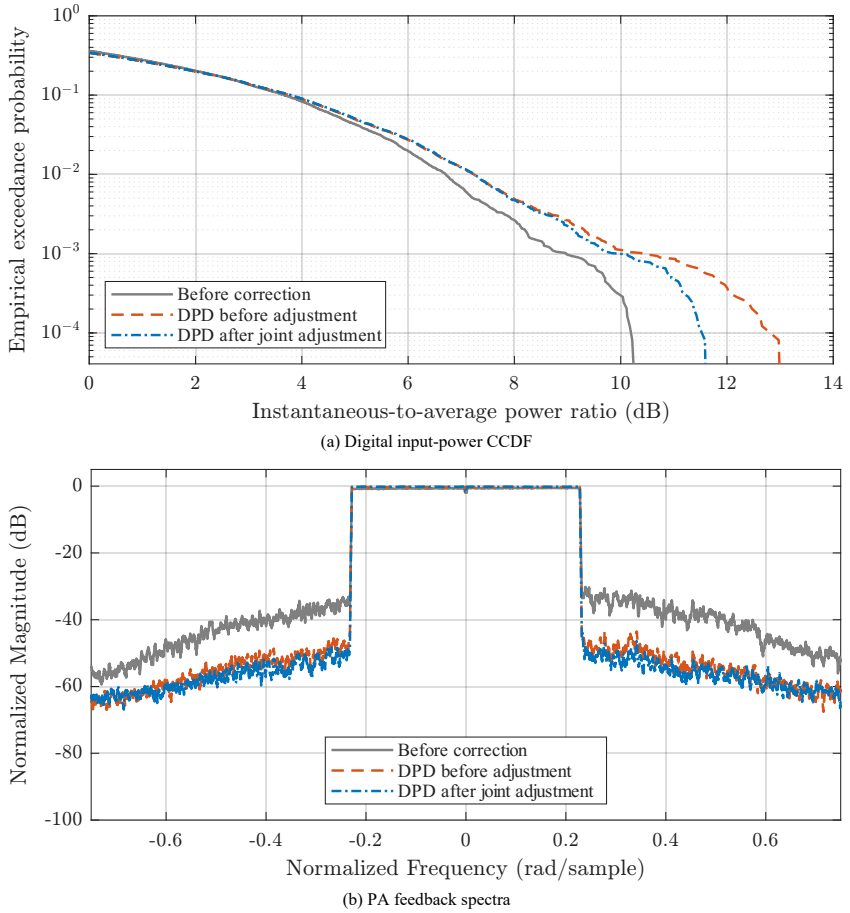


Fig. 8 Digital input-power distribution and PA feedback spectra. Three-state comparison before correction, with DPD before adjustment, and after joint adjustment. (a) Empirical CCDF of instantaneous-to-average digital input power. (b) Peak-normalized PA feedback spectra.

peak-normalized spectra are for visualization; Table 3 uses unsmoothed integrated powers for ACPR.

For comparison, bypassed CFR with $\lambda = 0.9999$ also meets the PAPR constraint, but gives PAPR of 11.999 dB and NMSE of -38.097 dB. The jointly selected configuration further reduces PAPR by 0.405 dB, improves NMSE by 0.440 dB, and improves upper and lower ACPR by 0.624/0.674 dB. Joint adjustment therefore improves PAPR, NMSE, and ACPR compared with forgetting-factor adjustment alone.

The joint adjustment improves NMSE and both adjacent-channel ratios while reducing DPD-output PAPR. The final PAPR is 0.907 dB below the trigger threshold.

6 Conclusions

This paper investigated the roles of PC-CFR and RLS identification in controlling peak regrowth after DPD. The digital studies show that stronger cancellation can greatly increase CFR waveform NMSE. Changing the forgetting factor modifies the identified predistorter and its peak regrowth. These observations motivate a sequential method that first retains the target PAPR immediately before NMSE first worsens. It then selects the forgetting factor with the lowest NMSE under the measured DPD-output PAPR constraint.

With the PA input-power and gain settings held fixed, a 10 dB target PAPR and $\lambda = 0.9999$ reduce DPD-output PAPR from 12.985 to 11.593 dB. PA feedback NMSE improves by 3.660 dB, while upper and lower ACPR improve by 2.554 and 2.416 dB. The result satisfies the default 12.5 dB trigger, and adding the specified 1 dB trigger margin updates the trigger to 12.593 dB for subsequent operation. The CCDF and PA feedback spectra illustrate the associated peak suppression and spectral improvement.

The measurements also show why further PAPR reduction is not necessarily preferable: stronger CFR can lower adjacent-channel power while increasing distortion relative to the original waveform. The selected point therefore reflects minimum NMSE under a PAPR constraint, with upper and lower ACPR retained to assess the spectral trade-off. The joint setting also improves on forgetting-factor adjustment alone for this input. These results demonstrate joint PAPR reduction and improved PA linearization under the measured operating condition.

List of abbreviations

ACPR, adjacent-channel power ratio; CCDF, complementary cumulative distribution function; CFR, crest factor reduction; CORDIC, coordinate rotation digital computer; DPD, digital predistortion; DUT, device under test; FIR, finite impulse response; FPGA, field-programmable gate array; LUT, lookup table; NMSE, normalized mean-square error; OFDM, orthogonal frequency-division multiplexing; PA, power amplifier; PAPR, peak-to-average power ratio; PC, personal computer; PC-CFR, peak-cancellation crest factor reduction; QPSK, quadrature phase-shift keying; RF, radio frequency; RLS, recursive least squares; Rx, receive; Tx, transmit.

Declarations

Availability of data and materials

The datasets used and/or analysed during the current study are available from the corresponding author on reasonable request.

Competing interests

The authors declare that they have no competing interests.

Funding

This research received no specific grant from any funding agency in the public, commercial, or not-for-profit sectors.

Authors' contributions

XW and FY contributed to the conceptualization and supervision of the study. RL developed the algorithms, performed the simulations and hardware experiments, analysed the data, and drafted the manuscript. YL contributed to the experimental

platform and methodology. YY contributed to data processing and validation. XW, FY, YL, and YY contributed to reviewing and revising the manuscript.

Use of AI-assisted tools

During the preparation of this manuscript, the authors used AI-assisted tools to assist with language polishing and translation, organization and consistency checking of existing research data, and comparison of methodological options. The authors reviewed and edited the AI-assisted content and take full responsibility for the final manuscript.

Acknowledgements

Not applicable.

References

[1] S.H. Han, J.H. Lee, An overview of peak-to-average power ratio reduction techniques for multicarrier transmission. IEEE Wireless Communications **12**(2), 56–65 (2005). https://doi.org/10.1109/MWC.2005.1421929

[2] R.J. Baxley, C. Zhao, G.T. Zhou, Constrained clipping for crest factor reduction in OFDM. IEEE Transactions on Broadcasting **52**(4), 570–575 (2006). https://doi.org/10.1109/TBC.2006.883301

[3] M. Mounir, M.B. El_Mashade, S. Berra, G.S. Gaba, M. Masud, A novel hybrid precoding-companding technique for peak-to-average power ratio reduction in 5G and beyond. Sensors **21**(4), 1410 (2021). https://doi.org/10.3390/s21041410

[4] A. Borel, V. Barzdėnas, A. Vasjanov, Linearization as a solution for power amplifier imperfections: A review of methods. Electronics **10**(9), 1073 (2021). https://doi.org/10.3390/electronics10091073

[5] S. Wang, M. Roger, C. Lelandais-Perrault, Impacts of crest factor reduction and digital predistortion on linearity and power efficiency of power amplifiers. IEEE Transactions on Circuits and Systems II: Express Briefs **66**(3), 407–411 (2019). https://doi.org/10.1109/TCSII.2018.2855084

[6] Z. Liu, X. Hu, W. Wang, F.M. Ghannouchi, A low-complexity joint PAPR reduction and predistortion based on generalized memory polynomial model. IEEE Microwave and Wireless Components Letters **32**(1), 88–91 (2022). https://doi.org/10.1109/LMWC.2021.3113666

[7] T. Kageyama, O. Muta, H. Gacanin, Performance analysis of OFDM with peak cancellation under EVM and ACLR restrictions. IEEE Transactions on Vehicular Technology **69**(6), 6230–6241 (2020). https://doi.org/10.1109/TVT.2020.2982587

[8] S. Trampitsch, M. Kalcher, H. Enzinger, D. Gruber, M. Lunglmayr, M. Huemer, A Circuit-Inspired Digital Predistortion of Supply Network Effects for Capacitive RF-DACs. IEEE Transactions on Microwave Theory and Techniques **69**(1), 271–283 (2021). https://doi.org/10.1109/TMTT.2020.3022382

[9] S.i. Hong, K.P. Lee, E.R. Jeong, Robust digital predistortion in saturation region of power amplifiers. International Journal of Electrical and Computer Engineering (IJECE) **6**(1), 99–105 (2016). https://doi.org/10.11591/ijece.v6i1.pp99-105

[10] C. Tarver, A. Balatsoukas-Stimming, C. Studer, J.R. Cavallaro, *Virtual DPD Neural Network Predistortion for OFDM-Based MU-Massive MIMO*, in *2021 55th Asilomar Conference on Signals, Systems, and Computers* (2021), pp. 376–380. https://doi.org/10.1109/IEEECONF53345.2021.9723343

[11] Y. Wu, G.D. Singh, M. Beikmirza, L.C.N. de Vreede, M. Alavi, C. Gao, *OpenDPD: An Open-Source End-to-End Learning & Benchmarking Framework for Wideband Power Amplifier Modeling and Digital Pre-Distortion*, in *2024 IEEE International Symposium on Circuits and Systems (ISCAS)* (2024), pp. 1–5. https://doi.org/10.1109/ISCAS58744.2024.10558162

[12] P.L. Gilabert, R.N. Braithwaite, G. Montoro, Beyond the moore-penrose inverse: Strategies for the estimation of digital predistortion linearization parameters. IEEE Microwave Magazine **21**(12), 34–46 (2020). https://doi.org/10.1109/MMM.2020.3023220

[13] S. Wang, M. Roger, J. Sarrazin, C. Lelandais-Perrault, A Joint Crest Factor Reduction and Digital Predistortion for Power Amplifiers Linearization Based on Clipping-and-Bank-Filtering. IEEE Transactions on Microwave Theory and Techniques **68**(7), 2725–2733 (2020). https://doi.org/10.1109/TMTT.2019.2956036

[14] S. Wang, M. Roger, J. Sarrazin, C. Lelandais-Perrault, Augmented Iterative Learning Control for Neural-Network-Based Joint Crest Factor Reduction and Digital Predistortion of Power Amplifiers. IEEE Transactions on Microwave Theory and Techniques **68**(11), 4835–4845 (2020). https://doi.org/10.1109/TMTT.2020.3011152

[15] Q. Zhang, R. Han, C. Jiang, J. Wang, H. Chang, F. Liu, End-to-end joint optimization for PAPR reduction and digital predistortion based on neural network. IEEE Microwave and Wireless Technology Letters **35**(5), 509–512 (2025). https://doi.org/10.1109/LMWT.2025.3546643

[16] S. Wang, P. Maris Ferreira, A. Benlarbi-Delai, Physics informed spiking neural networks: Application to digital predistortion for power amplifier linearization.

IEEE Access **11**, 48441–48453 (2023). https://doi.org/10.1109/ACCESS.2023.3275434

[17] W. Jing, J. Jin, Y. Fei, An enhanced peak cancellation algorithm for PAPR reduction with variable coefficient length and recoverable leak peak. IEEE Access **13**, 149158–149173 (2025). https://doi.org/10.1109/ACCESS.2025.3600489

[18] D. López, P.L. Gilabert, G. Montoro, N. Bartzoudis, *Peak Cancellation and Digital Predistortion of High-Order QAM Wideband Signals for Next Generation Wireless Backhaul Equipment*, in *2014 International Workshop on Integrated Nonlinear Microwave and Millimetre-Wave Circuits (INMMiC)* (2014), pp. 1–3. https://doi.org/10.1109/INMMIC.2014.6815111

[19] Analog Devices, Inc., *UG-2358 (Rev. 0): Reference Manual ADRV9042*. Analog Devices, Inc., rev. 0 edn. (2025). URL https://www.analog.com/media/en/technical-documentation/user-guides/adrv9042-reference-manual-ug-2358.pdf. Accessed 15 September 2026

[20] S.S.K.C. Bulusu, P. Susarla, H. Shaiek, D. Roviras, O. Silvén, *Fast Convergence Joint Optimization of PAPR Reduction and Digital Predistortion in the Next-Generation Broadcasting Systems*, in *2023 IEEE International Symposium on Broadband Multimedia Systems and Broadcasting (BMSB)* (Beijing, China, 2023), pp. 1–6. https://doi.org/10.1109/BMSB58369.2023.10211439

[21] A.L. Bruce, A. Goel, D.S. Bernstein, Convergence and consistency of recursive least squares with variable-rate forgetting. Automatica **119**, 109052 (2020). https://doi.org/10.1016/j.automatica.2020.109052

[22] A. Stotsky, Recursive least squares estimation with rank two updates. Automatika **66**(4), 619–624 (2025). https://doi.org/10.1080/00051144.2025.2517431

[23] C. Crespo-Cadenas, M.J. Madero-Ayora, J.A. Becerra, Upgrading behavioral models for the design of digital predistorters. Sensors **21**(16), 5350 (2021). https://doi.org/10.3390/s21165350

[24] W. Song, G. Wang, *Application of Recursive Least Squares Method with Variable Forgetting Factor in Digital Predistortion*, in *Second International Conference on Electronic Information Technology (EIT 2023)* (SPIE, Wuhan, China, 2023), p. 113. https://doi.org/10.1117/12.2685721

[25] W. Song, G. Wang, J. Ye, A Novel Digital Predistortion Identification Algorithm Based on Variable Forgetting Factor Recursive Least Square Method. International Journal of RF and Microwave Computer-Aided Engineering **2023**(1), 6377941 (2023). https://doi.org/10.1155/2023/6377941